Editors' Suggestion

Strong magnetoresistance in a graphene Corbino disk at low magnetic fields

Masahiro Kamada,[1] Vanessa Gall,[2,3] Jayanta Sarkar,[1] Manohar Kumar,[1,4] Antti Laitinen,[1]
Igor Gornyi,[2,3,5] and Pertti Hakonen[1,4,*]

[1]*Low Temperature Laboratory, Department of Applied Physics, Aalto University School of Science, P.O. Box 15100, 00076 Aalto, Finland*
[2]*Institute for Quantum Materials and Technologies, Karlsruhe Institute of Technology, 76021 Karlsruhe, Germany*
[3]*Institut für Theorie der Kondensierten Materie, Karlsruhe Institute of Technology, 76128 Karlsruhe, Germany*
[4]*QTF Centre of Excellence, Department of Applied Physics, Aalto University, P.O. Box 15100, 00076 Aalto, Finland*
[5]*Ioffe Institute, 194021 St. Petersburg, Russia*

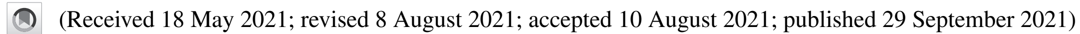

(Received 18 May 2021; revised 8 August 2021; accepted 10 August 2021; published 29 September 2021)

We have measured magnetoresistance of suspended graphene in the Corbino geometry at magnetic fields up to $B = 0.15$ T, i.e., in a regime uninfluenced by Shubnikov–de Haas oscillations. The low-temperature relative magnetoresistance $[R(B) - R(0)]/R(0)$ is strong, approaching 100% at the highest magnetic field studied, with a quite weak temperature dependence below 30 K. A decrease in the relative magnetoresistance by a factor of two is found when charge carrier density is increased to $|n| \simeq 3 \times 10^{10}$ cm^{-2}. Furthermore, we find a shift in the position of the charge neutrality point with increasing magnetic field, which suggests that magnetic field changes the screening of Coulomb impurities around the Dirac point. The gate dependence of the magnetoresistance allows us to characterize the role of scattering on long-range (Coulomb impurities, ripples) and short-range disorder (adatoms, atomic defects), as well as to separate the bulk resistance from the contact one. Based on the analysis of the magnetoresistance, we propose a more reliable method to extract the bulk mobility, which does not require prior knowledge of the contact resistance. It is thus demonstrated that studying magnetoresistance in the Corbino geometry is an extremely valuable tool to characterize high-mobility graphene samples, in particular, in the vicinity of the Dirac point.

DOI: 10.1103/PhysRevB.104.115432

I. INTRODUCTION

Besides extraordinary physical characteristics, graphene exhibits superb electrical transport properties [1,2]. Charge carrier conduction in monolayer graphene can display ballistic behavior over several microns, though the mean free path is often limited by Coulomb scattering and short-range scatterers [3]. Typically Coulomb scatterers, embedded in the substrate or caused by fabrication residues, dominate the transport and short-range scattering becomes important only at large carrier densities. Using freely suspended graphene flakes and current annealing [4], however, carrier scattering resulting from charged impurities and short-range defects can be minimized, and intrinsic properties of graphene can be observed. Many of the basic transport properties of graphene have been revealed using suspended devices. Suspended graphene in Corbino-ring geometry, for example, has turned out to be valuable in sensitive investigations of fractional quantum Hall states in graphene [5].

Magnetoresistance (dependence of resistance on magnetic field) is a powerful tool for studying basic quantum transport in monolayer graphene [2,6–9]. Typically, the resistance of graphene at low temperatures is governed by disorder-induced scattering, while at higher temperatures electron-electron and electron-phonon scattering start dominating. Disorder also leads to quantum corrections to the conductance and universal conductance fluctuations; such quantum effects are particularly sensitive to the presence of magnetic field. For classical magnetoresistance, both linear and quadratic behavior is expected according to effective medium theory [10,11]. Owing to strong demand for magnetic field sensors based on magnetotransport, various ways to generate large magnetoresistance in graphene have been developed in monolayer [9,12–21] and multilayer graphene [22,23]. In this work, we demonstrate that intrinsic behavior of suspended graphene in the Corbino-ring geometry, which already as such yields a strong magnetoresistance. This magnetoresistance can serve as an efficient tool for sample characterization as well as it can be used for sensing purposes. Our work demonstrates a magnetic field sensitivity on the order of 60 nT/$\sqrt{\text{Hz}}$ at 4 K in a background field of 0.15 T. For a detailed investigation of noise in the suspended-graphene Corbino samples studied in the present work, see Ref. [24].

In the Hall bar geometry, both the transverse and longitudinal bulk conductivities—$\sigma_{xy}(B)$ and $\sigma_{xx}(B)$, respectively—determine the resistivity $\rho_{xx}(B)$. As a result, $\rho_{xx}(B)$ turns out to be independent of the applied magnetic field B in the simplest one-band model. The Corbino-ring measurement setting for magnetoresistance is special already for this simplest case, because the Hall conductivity σ_{xy} (or the Hall voltage) drops out from the resistivity. The latter is then obtained just as the inverse of the longitudinal conductivity $\rho_{xx}(B) = 1/\sigma_{xx}(B)$. In a way, a Corbino disk is equivalent to an infinitely wide

*pertti.hakonen@aalto.fi

 ©2021 American Physical Society

sample, in which the effect of the sidewalls can be neglected. The magnetoresistance for generic anisotropic Corbino samples is calculated in Ref. [25]; in the isotropic case, relevant to our setup, the resistance of the Corbino sample is expressed through to the bulk resistivity as

$$R(B) = \frac{1}{2\pi}\,\rho_{xx}(B)\,\ln\frac{r_{\rm out}}{r_{\rm in}}. \quad (1)$$

Here $r_{\rm in}$ and $r_{\rm out}$ are, respectively, the inner and outer radii of the disk. The logarithmic geometrical factor in Eq. (1) reflects the total current conservation in the Corbino disk.

Bulk magnetoresistance measured in disordered graphene in the Hall-bar geometry may display complex magnetic-field dependence [26–29] for different sources of disorder potential; for example, indications of $\sqrt{B}$ dependence at small fields have been reported [30,31]. Our results, on the contrary, display a strong parabolic (B^2) magnetoresistance for arbitrary disorder, while only small corrections to the B^2 dependence are found for magnetic fields up to 0.1 T.

II. SAMPLE FABRICATION AND CHARACTERIZATION

Our graphene samples were fabricated using a technique based on lift off resist (LOR) sacrificial layer [32]; details of the employed process can be found in Ref. [5]. The current annealing of the samples at low temperature before measurements guaranteed a high maximal field-effect mobility $\mu_{\rm FE}^{\rm max} \simeq 1\text{–}2 \times 10^5$ cm^2/V s; see Sec. SI of the Supplemental Material (SM), Ref. [33]. Most of the data was measured on a Corbino disk with inner and outer radii of 0.9 and 2.25 μm, respectively. A false-color scanning electron microscope picture of a Corbino sample is displayed in Fig. 1(a), which is further clarified by the cross sectional view in Fig. 1(b). The employed two-lead measurement configuration with its connections is also outlined in Fig. 1(b). The gate capacitance $C_g = 1.5 \times 10^{-5}$ F/m^2 between the suspended graphene and Si^{++}-doped back gate was obtained using the Landau level fan diagram [5]. Note that the value of C_g is approximately by a factor of eight smaller than a typical back gate capacitance having just a 300-nm-thick SiO_2 dielectric. This large difference arises from the 500-nm vacuum gap due to the thickness of doubly spun LOR (2×250 nm).

In our experiments, we employed standard voltage-biased measurements and recorded current through the sample over the bias range of 1–13 mV. These rather large voltages were chosen in order to measure the low-frequency noise spectra simultaneously and the resistance noise of our samples was in the range of $\delta R/R \lesssim 2 \times 10^{-5}$ at 1 Hz. The current was amplified using a transimpedance amplifier at gain 10^5 V/A. Bias-T components facilitated insertion of rf signals to the sample. For details of the measurement system, see Ref. [34]. In the measurements, both positive and negative bias voltages V were used. A weak V dependence was removed by extrapolating data at $V < 0$ and at $V > 0$ down to zero bias: the two extrapolations differed less than 3%.

First, we characterized the gate voltage dependence of the resistance $R(V_g)$ of our sample at $B = 0$ (see lowest curves in Fig. 2) at two temperatures, $T = 4$ K and $T = 27$ K. The offset of the Dirac point from zero amounted to $V_g^D(0) \simeq 0.2$ V at $T = 27$ K, and the corresponding residual charge

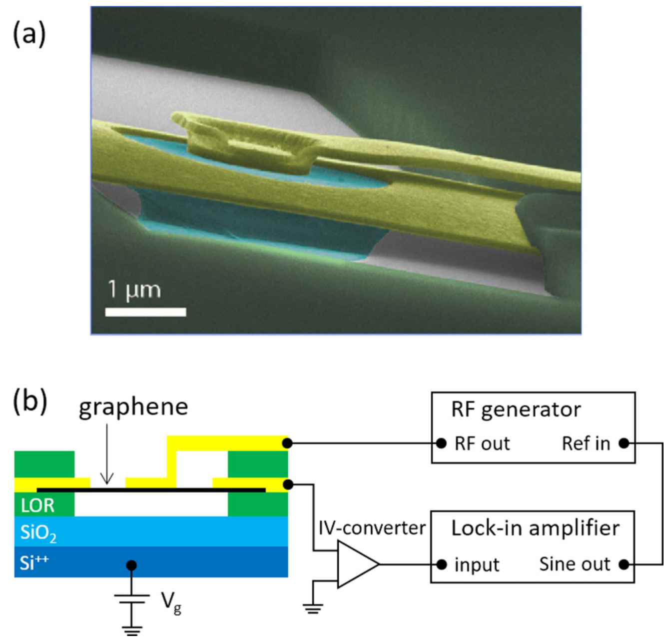

FIG. 1. (a) Scanning electron microscope image of a suspended graphene Corbino disk (green part in the center) with 4.5 μm diameter outer Au contact and 1.8 μm diameter inner Au contact; the scale is given by the white bar. (b) Cross-sectional view of the sample and its basic two-lead measurement connections. The thicknesses of the SiO_2 and LOR layers amount to 285 nm and 500 nm, respectively.

density was found to be $n_0 \simeq 8 \times 10^9$ cm^{-2}. For $T = 4$ K, the zero-B offset of the Dirac point had the opposite sign: $V_g^D(0) \simeq -0.2$ V. The temperature dependence of the offset (and, in particular, the change of its sign) can be related to different concentrations of (quasi)resonant adsorbed atoms; see below.

Figure 2 includes also our data at small magnetic fields, $B < 0.15$ T. For both temperature values, the resistance grows strongly with B and, simultaneously, there appears a shift of the maximum value to slightly higher gate voltage $V_g^D(B)$. The data points were joined using cubic spline fits in order to make observed changes with B easier to distinguish. According to the spline fits, the shift of the Dirac point for $T = 27$ K amounts to $\Delta V_g = V_g^D(B) - V_g^D(0) = 5(B/\mathrm{T})$ V. Even stronger shift is seen for $T = 4$ K. In both curves, there is a finite electron-hole asymmetry. The main contribution to this asymmetry is through the contact resistance at the leads, where a pn interface forms, which influences electrons and holes in graphene differently [35].

The observed shift of the Dirac point with increasing B can be attributed to changes in screening of charged impurities in a magnetic field near charge neutrality; see Sec. SII of SM [33] for more details. In this case, the total charge density induced on the membrane is less at the Dirac point at finite B, which would indicate generation of more positive charge on graphene by the screening. Thus the screening should take place by positive carriers and the impurities are negatively charged. In addition, there was a slow shift of the Dirac point position towards positive V_g over time (on the order of 0.2 V in one month). It is worth noting that the effect of magnetic field on screening is suppressed at higher densities and higher

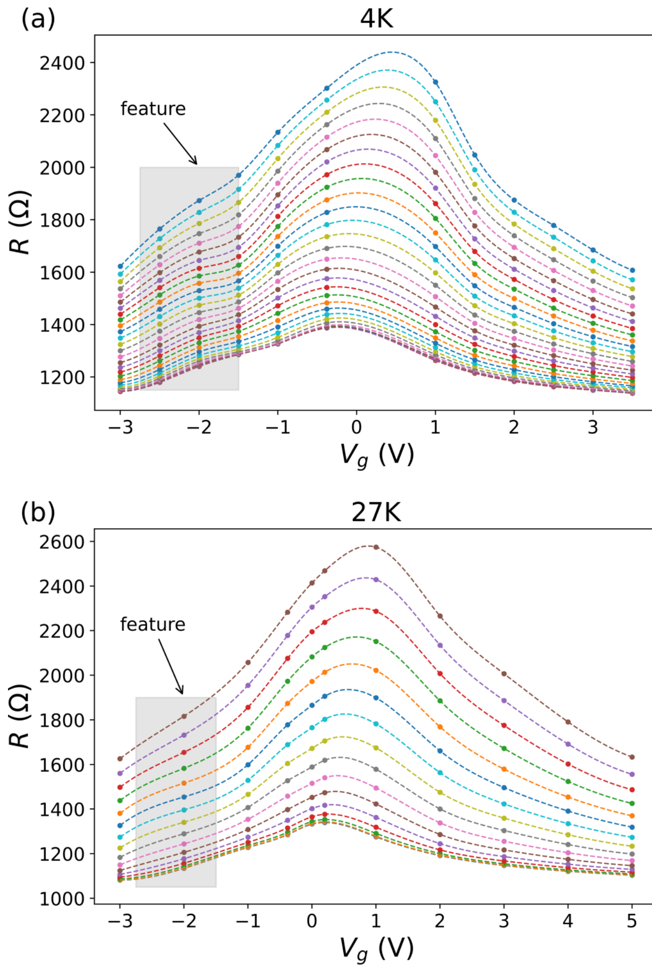

FIG. 2. Resistance vs V_g at various magnetic fields. (a) 4 K for magnetic fields from 0 to 0.15 T with 0.005 T step (from bottom to top); the broken curves are cubic spline interpolations to the data. (b) 27 K for magnetic fields from 0 to 0.15 T with 0.01 T step (from bottom to top); the broken curves are cubic spline interpolations. The gray area marks the region of increased resistance due to a broadened resonance level at V_g near −2 V (the feature is more pronounced at $T = 4$ K).

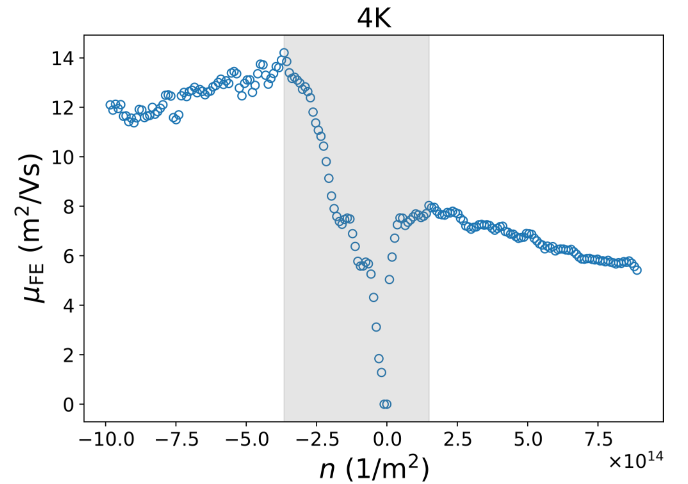

FIG. 3. Field effect mobility μ_{FE} at $T = 4$ K determined from the measured differential resistance dV/dI at $B = 0$. The Dirac point shift $V_g^D(0)$ has been subtracted off from the gate voltage before calculating the charge carrier density n. The dip in μ_{FE} around $n = 0$, indicated by a gray shadow, corresponds to the density range governed by disorder broadening of the Dirac point. The extent of this range is consistent with the value n_* given in Table I.

temperatures. This is in line with the stronger shift of the resistance maximum at $T = 4$ K.

One more peculiarity seen in the resistance curves plotted over the gate voltage is a feature close to −2 V, which is marked by a gray region for both temperatures shown in Fig. 2. The resistance around this voltage is somewhat enhanced compared to the resistance away from this voltage. There is no comparable feature at the electron side of the resistance curve and the feature is stronger for lower temperatures. We attribute this feature to a broadened resonance level associated with adsorbed local impurities. When the chemical potential is moved by the gate voltage into the vicinity of this quasiresonance, the scattering amplitude for such impurities is enhanced, leading to shorter transport scattering time and, hence, to the increase in resistance. At the same time, the broadening of this resonance is sufficiently strong to avoid truly resonant scattering (as, e.g., in the case of vacancies); in contrast to infinitely strong impurities (vacancies), the position of the quasiresonance is shifted away from the Dirac point. Away from the resonant energy, these impurities produce weak short-ranged disorder.

For higher temperatures, some adsorbed dirt is thermally removed form the sample, leading to a less pronounced feature. This suggests that the role of scattering off short-range disorder at higher temperatures could be decreased. Below, based on the analysis of the magnetoresistance curves, we will discuss this issue in more detail. The dependence of the concentration of local quasiresonant impurities on temperature can also explain the T dependence of zero-B shift of the Dirac point mentioned above. Indeed, at higher temperature ($T = 27$ K in Fig. 2), the shift of the chemical potential is smaller, which is consistent with the above picture of lower concentration of adsorbed impurities.

In Sec. IV, we deduce charge carrier mobility from the measured geometric magnetoresistance. For comparison, we display in Fig. 3 the field-effect mobility defined by $\mu_{FE} = e^{-1} d\sigma_{xx}/dn$, obtained from measurements of differential resistance $R(V_g)$ at the end of the experiments. These data measured at $T = 4$ K indicate that, for our sample at a tiny bias voltage, the maximum mobility for holes $\mu_{FE} \simeq 13$ m^2/V s is clearly larger than that for electrons $\mu_{FE} \simeq 7$ m^2/V s. However, at the employed bias voltages 1–10 mV, the influence of the pn interface at positive gate voltages appears to be reduced and μ_{FE} for electrons and holes becomes almost equal. This corresponds to the much weaker electron-hole asymmetry in Fig. 2. From this strong dependence of the field-effect mobility on the contact resistance we conclude that this is not a reliable way of characterizing the bulk mobility of the sample. As we are going to demonstrate below, the analysis of the magnetoresistance in the Corbino geometry allows one to extract the genuine value of the bulk mobility.

III. THEORETICAL BACKGROUND

Before analyzing the obtained magnetoresistance data, we present in this section the basic facts about disorder-dominated transport in graphene (for the hydrodynamic—collision-dominated—transport, higher temperatures are typically required than those in our experiment, 50 K $< T <$ 150 K, while phonons become important at yet higher T [36]). Distinct from conventional electron gases in 2D semiconductor heterostructures, graphene displays a linear energy dispersion relation of the carriers, $\varepsilon_{\rm k} = \pm v\hbar k$. This leads to the linear-in-energy density of states in clean graphene:

$$\nu_0(\varepsilon) = \frac{N|\varepsilon|}{2\pi v_F^2 \hbar^2}, \tag{2}$$

where $v_F = 10^6$ m/s is the Fermi velocity, ε is the energy counted from the Dirac point, and $N = 4$ is the degeneracy due to spin and valley degrees of freedom. Following from this density of states, the charge density of carriers is given by

$$n = N\frac{\varepsilon_F^2}{4\pi\hbar^2 v_F^2}, \tag{3}$$

where ε_F is the Fermi energy. A consequence of the linear dispersion relation is that the cyclotron frequency ω_c becomes energy dependent [2]:

$$\omega_c(\varepsilon) = \frac{eB}{m_c(\varepsilon)} = \frac{\hbar}{m_c(\varepsilon)\ell_B^2}, \tag{4}$$

where B is the magnetic field and $m_c(\varepsilon) = \varepsilon/v_F^2$ is the cyclotron mass, also dependent on the energy, and where we have defined a magnetic length by $\ell_B = \sqrt{\hbar/eB}$.

The linear dispersion relation also influences the scattering and relaxation rates of charge carriers. We assume that the major contributions to resistance arise from short-range scattering (s) and Coulomb scattering (C) and adopt this mixed-disorder model [37] to describe the magnetoresistance. For the interpretation of the effect of charged scatterers, one should keep in mind that graphene is not perfectly flat, but has ripples [38–40]. The scattering off ripples is similar to that for charged impurities [36], so that their contribution is effectively included in our treatment of Coulomb scattering.

We first address scattering on the short-range impurity potential. We limit our discussion to not too high carrier densities for which the length scale d for random potential variations is smaller than the carriers' wavelength and larger than the interatomic spacing a, i.e., $a \ll d \ll \lambda$. For such disorder the intervalley scattering can be disregarded and the quantum τ_q and transport $\tau_{\rm tr}$ scattering times can be estimated using Fermi's golden rule [2,41]:

$$\tau_q^s(\varepsilon) = \frac{\hbar\gamma_s}{|\varepsilon|}, \quad \tau_{\rm tr}^s(\varepsilon) = 2\tau_q^s(\varepsilon), \tag{5}$$

where

$$\gamma_s = \frac{2\hbar^2 v_F^2}{n_{\rm imp}^s U_0^2}, \tag{6}$$

$n_{\rm imp}^s$ is the concentration of short-range impurities, and U_0 denotes the magnitude of the impurity potential. In what follows, we will characterize the strength of short-range disorder in the samples by the parameter γ_s which is energy independent. The difference between $\tau_{\rm tr}$ and τ_q is caused by the weak scattering anisotropy which originates from the spinor nature of the wave functions.

The scattering times for charged impurities can be brought to similar form (see SM [33], Sec. SIII), although the effective parameter γ_C is then, in general, a function of the energy and the Fermi energy, as well as temperature and magnetic field (through the corresponding dependence of screening of Coulomb impurities by charged carriers). Below, we mainly consider sufficiently low temperatures and magnetic fields, keeping only the energy dependence of γ_C:

$$\tau_q^C(\varepsilon) = \frac{\hbar\gamma_C'(\varepsilon,\varepsilon_F)}{|\varepsilon|}, \quad \tau_{\rm tr}^C(\varepsilon) = 2\frac{\hbar\gamma_C(\varepsilon,\varepsilon_F)}{|\varepsilon|}. \tag{7}$$

Here $\gamma_C(\varepsilon,\varepsilon_F)$ and $\gamma_C'(\varepsilon,\varepsilon_F)$ are functions of the effective coupling (graphene "fine-structure constant") $\alpha = e^2/(\hbar v_F \epsilon_\infty)$, with ϵ_∞ the background dielectric constant; see SM [33], Sec. SIII. In the absence of a screening environment and neglecting the renormalization of velocity by Coulomb interaction, the nominal value of this constant is $\alpha_0 = 2.2$. However, both the screening and renormalization [2] effects reduce this value. For intermediate values of α, the relation $\tau_{\rm tr}^C(\varepsilon) \approx 2\tau_q^C(\varepsilon)$, similar to Eq. (5), holds, but it is no longer exact.

The conductivity in zero magnetic field in the presence of only short-range scatterers is given by the Drude formula:

$$\sigma_{xx}^D = \sigma_0 = \frac{2e^2\gamma_s}{\pi\hbar}. \tag{8}$$

By comparing this with the typical conductivity of high-quality graphene samples, we observe that γ_s should be of the order of unity if impurities in high-mobility samples, such as ours, were short ranged (this estimate corresponds to measured quantum scattering time at $V_g = 10$ V and scaled to our measurement regime).

An important parameter for the magnetoresistance is the product $\omega_c\tau_q^s$, which describes the broadening of Landau levels. Since for short-range scatterers both ω_c and τ_q^s depend on energy [see Eqs. (4) and (5)], the parameter

$$x = \omega_c\tau_q^s = \frac{\gamma_s\hbar^2 v_F^2}{\varepsilon^2\ell_B^2} \tag{9}$$

can be either small or large, depending on the energy ε [29]. For scattering on Coulomb impurities, the quantum scattering time decreases linearly with energy $\varepsilon \propto \sqrt{n}$, which means that the parameter $x = \omega_c\tau_q^C$ becomes energy independent. The parameter x determines the dependence of the density of states $\nu(\varepsilon)$ of disordered graphene on magnetic field. Since the transport scattering time $\tau_{\rm tr}$ has the same energy dependence as τ_q, the same parameter x governs the quasiclassical bending of particle trajectories in magnetic field.

The general result for the longitudinal conductivity $\sigma_{xx}(\varepsilon)$ is given by Eq. (4.13) of Ref. [41]. Introducing the relative density of states $\tilde\nu(\varepsilon) = \nu(\varepsilon)/\nu_0(\varepsilon)$, where $\nu_0(\varepsilon)$ is the zero-field density of states, we write the conductivity kernel (conductivity of particles at energy ε) in terms of $\tilde\nu(\varepsilon)$ as

follows:

$$\sigma_{xx}(\varepsilon) = \sigma_0 \frac{\tilde{\nu}(\varepsilon)^2}{\tilde{\nu}(\varepsilon)^2 + [\omega_c(\varepsilon)\tau_{tr}(\varepsilon)]^2}, \quad (10)$$

where

$$\sigma_0 = \frac{e^2 v^2}{2}\tau_{tr}(\varepsilon_F)\nu(\varepsilon_F) \equiv \frac{e^2\gamma N}{2\pi\hbar}. \quad (11)$$

Here, we have introduced the dimensionless disorder strength γ that has a meaning of a dimensionless conductance per spin per valley. For the short-range disorder, $\gamma = \gamma^s$. In the presence of both short-range and Coulomb scatterers, the total transport time is determined by

$$\frac{1}{\tau_{tr}(\varepsilon)} = \frac{1}{\tau_{tr}^s(\varepsilon)} + \frac{1}{\tau_{tr}^C(\varepsilon)}, \quad (12)$$

and γ is related to the total transport scattering time, as given by Eq. (11).

The finite-temperature conductivity is given by the kernel (10) integrated with the derivative of the Fermi function $n_F(\varepsilon)$:

$$\sigma_{xx} = \int_{-\infty}^{\infty} d\varepsilon \left(-\frac{\partial n_F(\varepsilon)}{\partial\varepsilon}\right)\sigma_{xx}(\varepsilon), \quad (13)$$

At zero temperature, the derivative gives the δ function and the conductivity reduces to Eq. (10) with $\varepsilon \to \varepsilon_F$. At zero magnetic field it is given by σ_0 from Eq. (11). The temperature dependence of the Drude conductivity arises from the energy dependence in the kernel (10) when the thermal broadening of the δ function is taken into account. At low temperatures, $k_B T \ll \varepsilon_F$, the finite-T corrections to the zero-T result are small, and the measured conductivity is given approximately by $\sigma_{xx} \approx \sigma_{xx}(\varepsilon_F, T = 0)$. Under these conditions, if $\tilde{\nu}_0$ is independent of the magnetic field, the conductivity in a finite magnetic field can be written in the conventional Drude form:

$$\sigma_{xx}(B) = \frac{en\mu_0}{1 + (\mu_0 B)^2}, \quad (14)$$

where μ_0 is the mobility at $B = 0$, i.e.,

$$\mu_0 = \frac{\sigma_{xx}(B = 0)}{ne}. \quad (15)$$

As can be seen from the calculation of $\tilde{\nu}_0(\varepsilon)$ in Refs. [29,42], corrections to the density of states arising from the finite magnetic field can be neglected, as long as $x \ll 1$, which we will show is true over a large range of data in the present experiment.

Comparison with Eq. (10) shows that $\omega_c(\varepsilon)\tau_{tr}(\varepsilon)/\tilde{\nu}_0(\varepsilon)$ corresponds to $\mu_0 B$. This means that the Drude conductivity is given by

$$\sigma_{xx} \approx \frac{e^2\gamma N}{2\pi\hbar}\frac{1}{1 + \left(\frac{2e\gamma}{\pi\hbar n}\right)^2 B^2}, \quad (16)$$

which has finite temperature corrections that are detailed in the SM [33], Sec. SIV. There are also temperature-dependent quantum corrections to the Drude conductivity, in particular, those arising from the electron-electron interaction (EEI), as discussed in Sec. SV of SM [33].

For both short-range and Coulomb impurities, Eq. (10) then yields a parabolic magnetoresistance in the Corbino geometry. The Drude resistivity in the Corbino geometry takes a simple form:

$$\rho_{xx}(B) = \frac{1}{\sigma_0}[1 + (\mu_0 B)^2]. \quad (17)$$

According to the Mathiessen rule, the inverse mobility can be written as a sum of the contributions of different momentum-relaxing scattering processes,

$$\mu_0^{-1} = \mu_C^{-1} + \mu_s^{-1}, \quad (18)$$

which yields in the zero-T limit

$$\frac{1}{\mu_0} = \frac{\pi\hbar n}{2e\gamma} = \frac{\pi\hbar n}{2e}\left(\frac{1}{\gamma_s} + \frac{1}{\gamma_C(\varepsilon = \varepsilon_F, \varepsilon_F)}\right), \quad (19)$$

$$\gamma_C(\varepsilon = \varepsilon_F, \varepsilon_F) = \frac{n}{c(\alpha)n_{imp}^C}, \quad (20)$$

with $c(\alpha)$ defined in the SM [33], Sec. SIII. One sees that the contribution of Coulomb scatterers to the inverse mobility is density independent. On the other hand, the mobility governed by short-range impurities decreases with charge carrier density as $\mu_s \propto 1/n$. Thus the density dependence of the total mobility allows one to characterize the role of short-range and Coulomb impurities in transport.

Below a certain chemical potential or the corresponding density n_*, disorder-induced broadening smears the single-particles energy and the density of states saturates. This energy scale is given by the self-consistent equation for ε:

$$\frac{\hbar}{\tau_q(\varepsilon_*)} \sim \varepsilon_*. \quad (21)$$

For the mixed disorder model with $\gamma_s \gg 1$, we get for the corresponding density

$$n_* \sim d(\alpha)n_{imp}^C, \quad (22)$$

where $d(\alpha)$ is given in the SM [33], Sec. SIII. The value of n_* depends on the density of charged impurities, fine-structure constant α. We model this saturation effect by performing the replacement $n \to \sqrt{n^2 + n_*^2}$, which effectively interpolates between n at high densities and n^* at the neutrality point, in all formulas, when used for plotting or fitting. In order to keep the notation clear, we do not explicitly write down this replacement in the main text. Since this replacement is an approximate interpolation, it describes the behavior of the density of states (and other observables) at $n \sim n_*$ only qualitatively; see the Appendix for details. Nevertheless, this simple interpolation function allows us to confidently extract the system parameters, when the range of densities $n \gg n_*$ is included in the fit.

IV. ANALYSIS OF DATA AND RESULTS

The relative magnetoresistance

$$\Delta R(B)/R(0) = R(B)/R(0) - 1$$

of our sample at $B < 0.15$ T is illustrated in Fig. 4, which depicts the relative resistance $R(B)/R(0)$ as a function of B^2 measured at $T = 4$ K [Fig. 4(a)] and at $T = 27$ K [Fig. 4(b)].

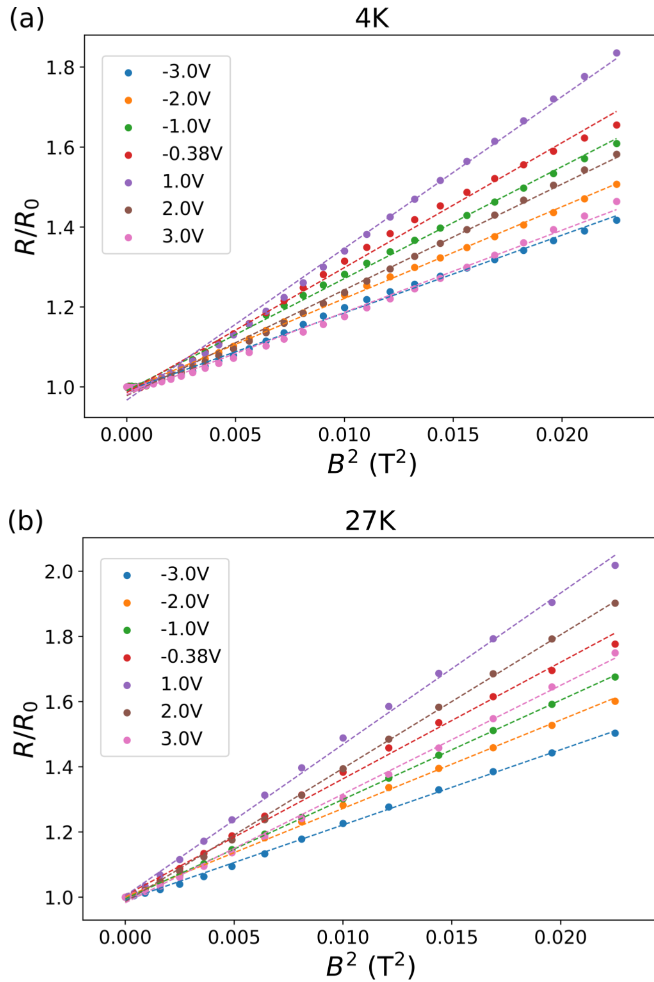

FIG. 4. (a) Scaled resistance $R/R(0)$ vs B^2 at $T = 4$ K measured at various gate voltage values V_g between -3 and $+3$ V (0.8×10^9 cm^{-2} < $|n| < 3 \times 10^{10}$ cm^{-2}). The Dirac point corresponds to $V_g \simeq 1$ V, the data at which is denoted by lilac symbols in the figure. The dashed curves are guides for the eye, emphasizing an overall parabolic magnetoresistance and slight deviations from parabolicity. (b) Scaled resistance $R/R(0)$ vs B^2 at $T = 27$ K measured at various gate voltage values between -3 and $+3$ V. The magnetoresistance at low fields grows faster at 27 K than at 4 K.

In both data sets, the magnetoresistance is found to be the strongest at the Dirac point, which is due to the strong dependence of the mobility on the inverse of the density and the weak (in the case of only short-range scattering—even absent) dependence of the effective coupling constant on density. Both data sets are influenced by the growing shift of the Dirac point ΔV_g as B increases.

The strength of the measured magnetoresistance depends only weakly on temperature up to 27 K. However, when comparing the data at 4 K and 27 K, one observes that the B^2 dependence is followed better at 27 K than at 4 K in small magnetic fields. Qualitatively, this could be a signature of the increased role of electron-electron scattering [28,29] and macroscopic inhomogeneities [11,31,43]. In our suspended graphene sample such inhomogeneities can be due to static ripples.

The nature of scattering does not appear to play a large role in the measured magnetoresistance. The parabolic field dependence is followed for both Coulomb and short-range impurities in the range of parameters covered: $|n| \sim 0.8$–3×10^{10} cm^{-2} and $T = 4$–27 K. In general, the B^2 dependence at small magnetic fields is more closely followed in the 27 K data. The 4 K data displays deviations from B^2 behavior at $B < 30$ mT, which may be a sign of coherent behavior and quantum interference effects, either regular weak localization type or Corbino-geometry related as predicted for graphene in Ref. [44]. At the largest magnetic fields around 0.1–0.15 T, small deviations from B^2 dependence become obvious, in particular near the Dirac point. One can interpret this deviation as the onset of the Shubnikov–de Haas (SdH) oscillation regime in the sample [45] that corresponds to $x \sim 1$.

On top of this one has to consider the additional contribution R_{cont} to the measured resistance related to the contact effects. These contributions are the resistance of the metal-graphene contacts and the interface resistance of the contact-doped graphene region. The former contribution is a microscopic material property, which we take to be constant. The latter, discussed in Ref. [35], is of the type of the *pn*-junction resistance. This contribution to the total resistance depends on the density of charge carriers in the bulk of the sample and is the main cause for the usually observed electron-hole asymmetry in transport measurements. In low magnetic fields the cyclotron radius is larger than the geometrical length scales characterizing the contact region and, hence, the overall contact resistance should not show a pronounced magnetic-field dependence.

The parabolic magnetoresistance is associated with the bulk contribution, whereas the total resistance includes the contact resistance: $R = R_{\text{bulk}} + R_{\text{cont}}$, where R_{bulk} describes the disorder-induced bulk resistance and R_{cont} the contact contribution. Since R_{cont} depends on the gate voltage, the normalized magnetoresistance shown in Fig. 4 is not particularly convenient for extracting the density dependence of the mobility. Indeed, the value of $R(B = 0)$ in the denominator of the scaled magnetoresistance is not equal to $R_{\text{bulk}}(B = 0)$ in front of the B-dependent term coming from Eq. (17), so that the coefficient in front of the B^2 term in the scaled magnetoresistance is not equal to μ_0^2.

To overcome this complication caused by the contact resistance, we have employed a fitting function of the form

$$R(B) - R(0) = MB^2 \tag{23}$$

of the total resistance, where we have a single fitting parameter M fully determined by the properties of the bulk of the sample. According to Eq. (17) we have $M = R_{\text{bulk}}(0)\mu_0^2$, where $R_{\text{bulk}}(0)$ describes bulk resistance at zero field and μ_0 is the mobility. We recall that $R_{\text{bulk}}(0)$ is different from the measured $R(0)$ because the latter includes the contact contribution. There is no mechanism leading to a strong magnetic-field dependence of the contact resistance in the range of magnetic fields where no skipping orbits (or edge states) appear at the interfaces between the sample and the leads. The fact that we are able to consistently fit the observed magnetoresistance using our model in a wide range of gate voltages supports this argument.

TABLE I. Parameters extracted from the fit of the data. These parameters are used in all following plots.

	$T = 4$ K	$T = 27$ K
γ_s	9.6	38.2
n_* (m^{-2})	1.7×10^{14}	1.8×10^{14}
$c(\alpha)n^C_{\text{imp}}$ (m^{-2})	1.1×10^{14}	0.88×10^{14}

Since magnetoresistance is related to mobility, the data can be employed to derive information on the impurity scattering in our sample from the obtained fitting parameter M, which is given by

$$M = R_{\text{bulk}}(0)\mu_0^2 = \frac{\gamma}{\pi^2\hbar n^2}\ln\frac{r_{\text{out}}}{r_{\text{in}}} = \frac{1}{\pi^2\hbar n^2}\left(\frac{1}{\gamma_s} + \frac{c(\alpha)n^c_{\text{imp}}}{n}\right)^{-1}\ln\frac{r_{\text{out}}}{r_{\text{in}}}. \qquad (24)$$

In order to include the disorder-induced saturation of the density of states, we replace n with $\sqrt{n^2 + n_*^2}$ in the fitting function, and then extract γ_s, n_*, and the effective concentration of Coulomb impurities $c(\alpha)n^C_{\text{imp}}$. We fit our data over the full measured voltage range, with all the results being electron-hole averaged. The values we extract from these fits are shown in Table I.

Notably, the energy corresponding to n_* is $\varepsilon_* \approx 9$ meV, which is larger than the energies corresponding to 4 K and 27 K, which are 0.3 meV and 2.3 meV, respectively, so that finite-T corrections are small, even for 27 K. Moreover, the value of n_* is consistent with the region corresponding to disorder broadening of the Dirac point in the field effect mobility shown in Fig. 3. In Fig. 5, we show a comparison of the shifted magnetoresistance and the corresponding fit by the theoretical curves obtained from Eq. (17) for various values of the gate voltage difference

$$U = V_g - V_g^D$$

relative to the gate voltage V_g^D corresponding to the Dirac point, with the fitting parameters from Table I. Voltage U and density n are connected by the capacitance as $n = C_gU/e$.

With the parameters obtained from fitting the magnetoresistance curves, we get the mobility from Eq. (19), see Fig. 6, where the inverse mobility μ_0^{-1} is displayed as a function of gate voltage difference U. A clear minimum is found at the Dirac point (maximum for the mobility). The slope of the inverse mobility away from the Dirac point is determined by the strength of short-range scatterers γ_s. We observe that, at $T = 27$ K, the mobility varies only very slightly as a function of the gate voltage. This indicates that the role of short-range impurities is suppressed at higher temperature. Possibly, with increasing temperature, residual dirt (adsorbed atoms) is removed from the sample.

For comparison, the insets in Fig. 6 show the mobility $\tilde{\mu}_0$ that could be naively extracted from the formula $R(B)/R(0) = 1 + \tilde{\mu}_0^2 B^2$. As mentioned above, this quantity is not the genuine bulk mobility μ_0, since $\tilde{\mu}_0$ includes the effect of the contact resistance. Note that $\tilde{\mu}_0$ reveals the electron-hole asymmetry. Moreover, we rather clearly see a feature on the hole side, stemming from the feature in the resistance mentioned at $V_g = -2V$ in Fig. 2. Since we extract this from the shifted data, $V_g = -2V$ is mapped to different U for each magnetic field and thus this feature is not as clearly localized anymore. Mobility obtained this way is lower, since it is affected by the contact-resistance contribution.

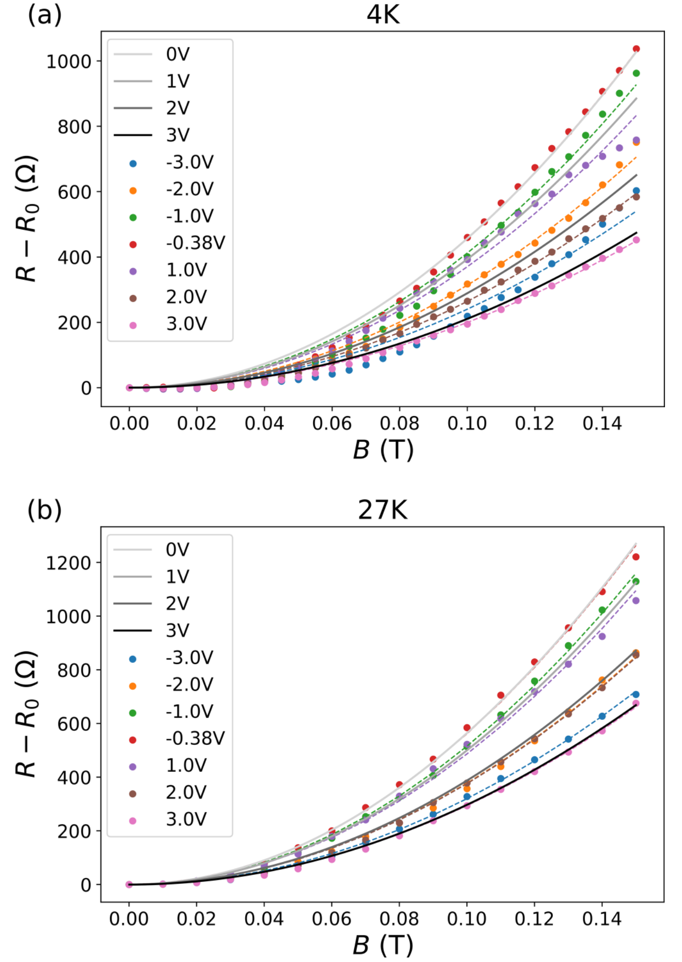

FIG. 5. Non-normalized magnetoresistance $R(B) - R(0)$ for 4 K in (a) and 27 K in (b) for various values of U. The points are obtained after shifting the gate voltage by V_g^D. The dashed lines correspond to the fitted function Eq. (23) and solid lines to theoretical zero-temperature magnetoresistance, Eq. (17), calculated using the parameters from Table I. Since these parameters are obtained at finite temperature and are electron-hole averaged, the dashed and solid lines do not exactly coincide for the same values of the gate voltage.

Thus, looking at the deduced impurity scattering strengths from the obtained mobilities, our magnetoresistance data should reflect effects related to both Coulomb and short-range scatterers. Note that our Hall mobility is slightly smaller than the field-effect mobility obtained using $R(V_g)$, which yields approximately 10^5 cm^2/V s near Dirac point for the average mobility of electrons and holes. The value of mobility extracted from the analysis of the magnetoresistance is consistent with the field-effect mobility.

Subtracting the disorder-induced bulk resistance with the parameters obtained from the measured magnetoresistance, we get access to the overall contact resistance, which is shown

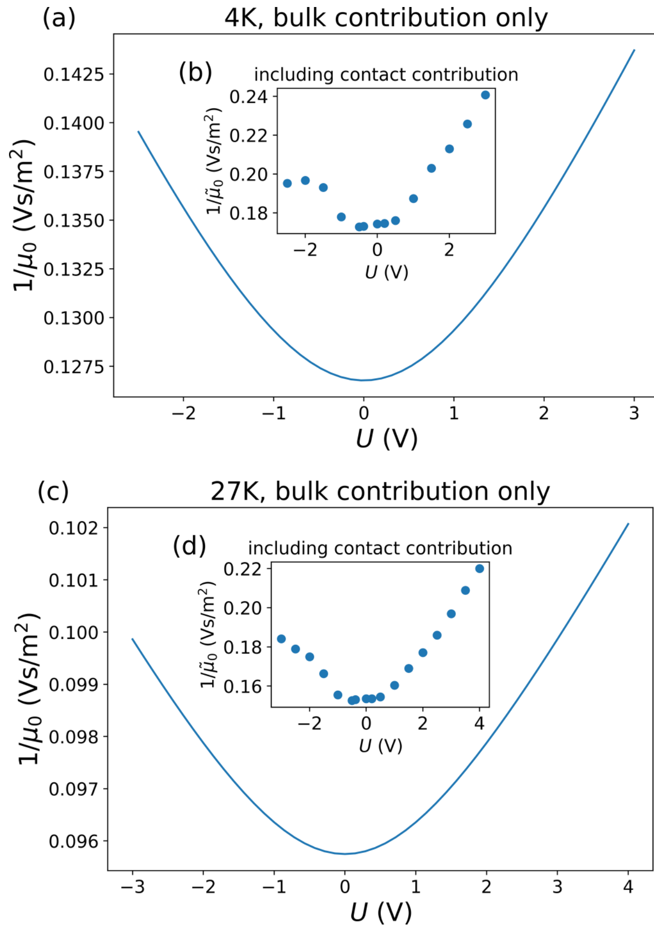

FIG. 6. (a) Electron-hole averaged inverse mobility, Eq. (19), derived using the parameters extracted from the 4 K magnetoresistance data. (b) Mobility naively extracted from the scaled shifted magnetoresistance as $R(B)/R(0) = 1 + \tilde{\mu}_0^2 B^2$: this includes the contribution of the contact resistance. (c) Inverse mobility derived from the 27 K data. Panel (d) as in (b) for 27 K. The parameters are given in Table I.

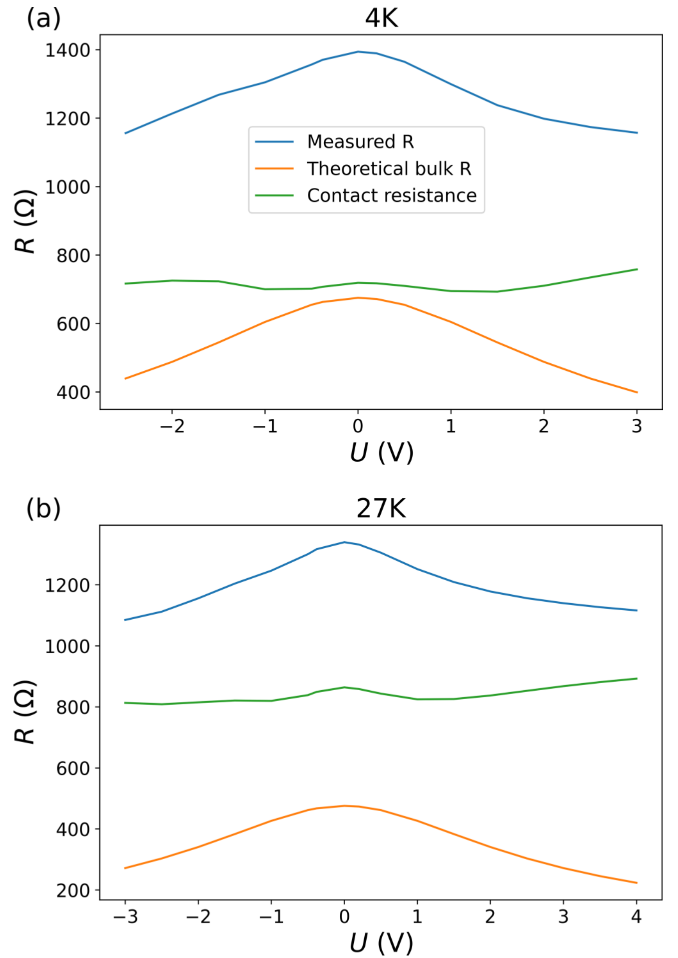

FIG. 7. Zero-B resistance at $T = 4$ K in (a) and $T = 27$ K in (b). Blue curves: the measured resistance. Orange curves: the zero-T bulk resistance calculated from Eq. (1) with the electron-hole averaged parameters from the fit (Table I). Green curves: the contact resistance which is obtained as the difference of the total measured resistance and the theoretical value of the bulk resistance. Note that the contact resistance is actually larger than the bulk contribution, as expected for high-mobility samples.

in Fig. 7. The obtained value of the contact resistance is somewhat higher than the one reported for similar samples in the Corbino geometry, which can be related to the fact that the sample has been cooled down several times and the contact structure on top of LOR resist is not very rigid around room temperature.

V. DISCUSSION AND CONCLUSIONS

In summary, we have investigated geometric magnetotoresistance in suspended graphene Corbino ring at low temperatures. The quadratic magnetoresistance $\Delta R(B)/R(0) \propto B^2$ is strong, approaching 100% at the highest magnetic field studied of 0.15 T at the Dirac point, with quite small temperature dependence below 30 K. This is comparable, in this range of magnetic fields, with the "extraordinary magnetoresistance" in encapsulated graphene in a disk geometry observed at room temperature in Ref. [9] (although the physical mechanism behind the low-temperature strong magnetoresistance is different). The relative magnetoresistance decreases with charge density and, at $|n| \simeq 3 \times 10^{-10}$ cm^{-2}, it is already reduced by a factor of two.

The simple zero-temperature analysis appears to be sufficient to explain the main features of the measured magnetoresistance. The quadratic magnetic field dependence is followed for both short-range and charged scatterers. The gate dependence of the magnetoresistance allows one to estimate the partial contributions of the short-range and long-range impurity scattering to the mobility. In particular, away from the Dirac point, the gate-voltage dependence of the mobility is entirely determined by the short-range component of the impurity potential. At the same time, we see that transport around the neutrality point is dominated by scattering on long-range disorder (Coulomb impurities or ripples). However, no fundamental difference is observed between Coulomb and short range in terms of the magnetic-field dependence of the resistance.

We find that the mobility extracted from the parabolic magnetoresistance is sufficiently high (of the order of 10^5 cm^2/V s), which is in agreement with previous estimates for similar (slightly cleaner) samples used for studying the quantum Hall effect, including the fractional quantum Hall effect. It is worth noting that, somewhat counterintuitively, the mobility is found to be higher at higher T. This can be related to the technological process of preparing the sample, where the concentration of adsorbed atoms depends on temperature. The total measured resistance is given by the sum of the bulk and contact contributions. We see that, in our geometry, the contact resistance is even higher than the bulk resistance, which is consistent with the high quality of the sample.

We emphasize that knowledge on the contact resistance is essential in the analysis of our geometric magnetoresistance. According to Eq. (24), the measured magnetoresistance is proportional to $R_{\text{bulk}}\mu_0^2B^2$, where $R_{\text{bulk}} = R - R_{\text{cont}}$. If we employed R instead of R_{bulk}, we would overestimate the reduction of μ_0 obtained from the magnetoresistance data as a function of gate voltage. For example, naively fitting the normalized data in Fig. 4(b) we would deduce a reduction in μ^2 by a factor of two, while from Fig. 6(b) we obtain only $<13\%$ reduction in μ^2. Thus, in the former case, the strength of the short-range scattering would appear almost three times larger than in the correct analysis.

In the vicinity of the Dirac point at 4 K, we find a high sensitivity of resistance variation with respect to magnetic field $dR/dB = 12.5$ kΩ/T at $B = 0.15$ T. According to our current-noise measurements [24] yielding $S_I = 10^{-23}$ A^2/Hz at 1 kHz for the same sample at 10 μA, we may estimate a magnetic field sensitivity of 60 nT/$\sqrt{\text{Hz}}$ for our device at 4 K. This sensitivity is excellent when compared with graphene Hall magnetometers, since our result is on par with magnetic field sensitivities of devices working in 20 times larger magnetic fields [46].

To conclude, the analysis of graphene magnetoresistance at different values of the gate voltage in the Corbino geometry allowed us to extract information about scattering mechanisms in the sample, and to separate the bulk and contact contributions to the resistance. The strong magnetoresistance of Corbino geometry at low magnetic fields appears to be a very powerful tool of characterization of the graphene samples. As an outlook, it will be very interesting to investigate experimentally and theoretically the magnetoresistance of graphene in this geometry at elevated temperatures, when electronic hydrodynamic effects become pronounced.

ACKNOWLEDGMENTS

We thank P. Alekseev, D. Golubev, and S.-S. Yeh for fruitful discussions and comments. This work was supported by the Academy of Finland Projects No. 314448 (BOLOSE), No. 310086 (LTnoise), and No. 312295 (CoE, Quantum Technology Finland), by ERC (Grant No. 670743), as well as by the DFG within FLAG-ERA Joint Transnational Call (Project No. GO 1405/5-1 GRANSPORT) and RFBR (Grant No. 20-02-00490). This research project utilized the Aalto University OtaNano/LTL infrastructure which is part of European Microkelvin Platform EMP (funded by European Union's Horizon 2020 Research and Innovation Programme Grant No. 824109).

APPENDIX: VICINITY OF THE DIRAC POINT AND DETAILS OF THE FITTING

As seen in Fig. 2, the resistance does not diverge at the Dirac point, as would be expected from combining the resistivity $\rho_0 = 1/\sigma_0$ from Eq. (11) with the effective γ from SM [33] (Sec. SIII) using γ_C as expressed in Eq. (20). The reason for this is the saturation of the density of states close to the Dirac point due to disorder [2,42]. Below a certain chemical potential μ_*, the quasiparticle pole in the Green's function is effectively absent, and all quantities should be fixed below this value. The relevant scale for this behavior is given by Eq. (21). In order to determine the changes this induces and find Eq. (22), we discuss here how to find the relevant scale μ_* from the condition

$$\frac{\hbar}{2\tau_q(\mu_*)} = \mu_*. \tag{A1}$$

Below μ_*, the density of states saturates, while it is not affected for larger energies, i.e.,

$$\nu(\varepsilon) = \begin{cases} \nu_*, & |\varepsilon| \ll \mu_*, \\ \nu_0(\varepsilon), & |\varepsilon| \gg \mu_*. \end{cases} \tag{A2}$$

This value enters directly into the calculation of all scattering rates Eq. (S2) of SM [33]; it also directly determines the screening radius in the Coulomb impurity case Eq. (S7) of SM [33]. While it is clear that Eq. (S2) of SM [33] is only true if the density of states is not strongly broadened, the idea is to approach the crossover from the side of large energies, where this is the case. We can then calculate the Coulomb scattering rates as follows:

$$\frac{1}{\tau_{\text{tr}}^C(\mu)} = \frac{\pi^2}{4}\hbar^3 v_F^4 n_{\text{imp}}^C c(\alpha) \begin{cases} \frac{\nu_*}{\mu_*^2}, & \mu \ll \mu_*, \\ \frac{\nu_0(\mu)}{\mu^2}, & \mu \gg \mu_*, \end{cases} \tag{A3}$$

$$\frac{1}{\tau_q^C(\mu)} = \frac{\pi^2}{4}\hbar^3 v_F^4 n_{\text{imp}}^C d(\alpha) \begin{cases} \frac{\nu_*}{\mu_*^2}, & \mu \ll \mu_*, \\ \frac{\nu_0(\mu)}{\mu^2}, & \mu \gg \mu_*, \end{cases} \tag{A4}$$

and, in a similar fashion, we get for short-range scatterers

$$\frac{1}{\tau_{\text{tr}}^s(\mu)} = \frac{1}{\gamma_s}\frac{\pi\hbar v_F^2}{4} \begin{cases} \nu_*, & \mu \ll \mu_*, \\ \nu_0(\mu), & \mu \gg \mu_*, \end{cases} \tag{A5}$$

$$\frac{1}{\tau_q^s(\mu)} = \frac{1}{\gamma_s}\frac{\pi\hbar v_F^2}{2} \begin{cases} \nu_*, & \mu \ll \mu_*, \\ \nu_0(\mu), & \mu \gg \mu_*. \end{cases} \tag{A6}$$

By assuming that the expression for $\mu \gg \mu_*$ is still reasonably close for $\mu \sim \mu_*$ and using both short-range and Coulomb impurities in Eq. (A1) we find

$$\mu_* = \sqrt{\frac{\pi}{2} v^2\hbar^2 d(\alpha)\frac{n_{\text{imp}}^C}{2 - 1/\gamma_s}}, \quad n_* = \frac{d(\alpha) n_{\text{imp}}^C}{4 - 2/\gamma_s}, \tag{A7}$$

which leads to the approximation Eq. (22). This value depends on the density of charged impurities and γ_s. The effective γ can then be extracted from the definition of γ, Eq. (11). We see that the density of states actually drops out; only the influence of $\nu(\varepsilon)$ on the electronic density (via μ^2) is relevant. We find

the required asymptotics

$$\frac{1}{\gamma} = \frac{1}{\gamma_s} + \begin{cases} \frac{c(\alpha)n_{\text{imp}}^C}{n_*}, & n \ll n_*, \\ \frac{c(\alpha)n_{\text{imp}}^C}{n}, & n \gg n_*, \end{cases} \tag{A8}$$

which we phenomenologically fulfill by tweaking the relation between density and chemical potential in graphene to

$$\sqrt{n^2 + n_*^2} = N\frac{\mu^2}{4\pi\hbar^2 v^2}, \tag{A9}$$

and consequently we replace n by $\sqrt{n^2 + n_*^2}$ in all fits and plots, as mentioned in the main text.

Using the general conductivity formula (16) with the finite disorder broadening, Eq. (A9), we get the broadened form of Eq. (19) and Eq. (20):

$$\frac{1}{\mu_0} \approx \frac{\pi\hbar}{2e}\left(\frac{\sqrt{n^2 + n_*^2}}{\gamma_s} + c(\alpha)n_{\text{imp}}^C\right) \tag{A10}$$

and

$$\frac{1}{\gamma} = \frac{1}{\gamma_s} + \frac{c(\alpha)n_{\text{imp}}^C}{\sqrt{n^2 + n_*^2}}. \tag{A11}$$

Let us now discuss how the fits are performed and obtain the parameters for Table I. The first step is to remove the Dirac point shift as discussed in the SM [33], Sec. SII. In practice, we do not employ the inhomogeneous shift introduced there, but rather just shift the curves as a whole, such that the maximum is at zero voltage. From the cubic spline through the measured data points, we read off the resistance values at the original voltages and additionally all half integer ones for 27 K.

We then fit the obtained magnetoresistances $R(B) - R(0)$ over the whole measured range of B with the fit function Eq. (23) for all gate voltages. From the thus obtained parameter M we extract all parameters of the theory according to Eq. (24). We fit the magnetoresistance with three parameters

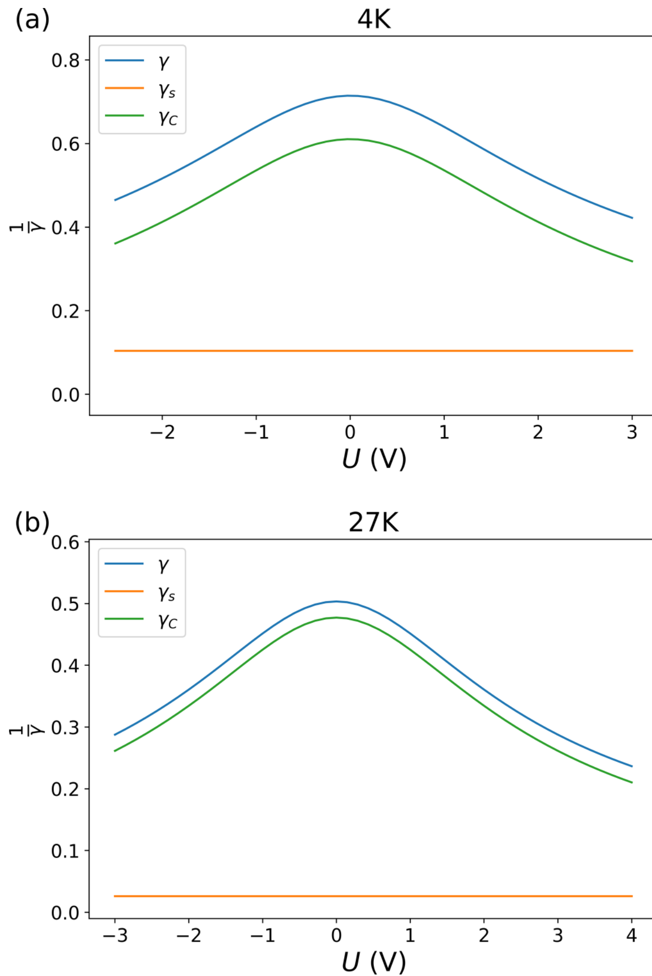

FIG. 8. Effective disorder parameter $1/\gamma$ defined by Eq. (A11) and its two parts $1/\gamma_C$ and $1/\gamma_s$ for $T = 4$ K (a) and $T = 27$ K (b). The parameter γ is smaller for 4 K, which means that disorder is stronger at lower temperatures. The parameters are given in Table I.

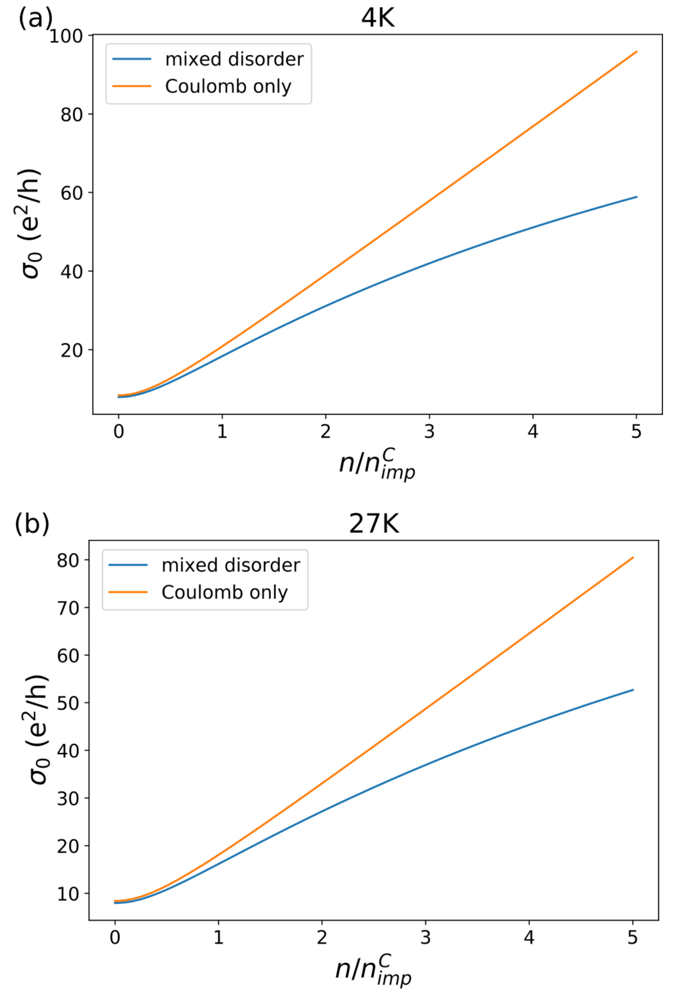

FIG. 9. (a) Conductivity at $B = 0$ T, Eq. (11), derived using the parameters extracted from the 4 K magnetoresistance data. (b) Zero-field conductivity derived from the 27 K data. The blue curve is the result for our mixed disorder model and the orange one for $\gamma_s = \infty$, i.e., no short-range scatterers. The parameters are given in Table I; additionally, we used $\alpha = 1.3$ to determine n_{imp}^C.

γ_s, $c(\alpha)n_{\text{imp}}^C$, and n_*, expressing M as follows:

$$\frac{1}{M} = \pi^2\hbar(n^2 + n_*^2)\left[\frac{1}{\gamma_s} + \frac{c(\alpha)n_{\text{imp}}^C}{\sqrt{n^2+n_*^2}}\right]. \quad \text{(A12)}$$

A plot of the resulting effective disorder parameters γ for the two temperatures is shown in Fig. 8.

In order to summarize the effect of the two different types of impurities, in Fig. 9 we show the zero-field conductivity σ_0 determined by Eq. (11) for both our mixed disorder model and a Coulomb-impurity model. Already at experimentally accessible density ratios $n/n_{\text{imp}}^C \approx 2$ we observe the sublinear conductivity due to short-range scatterers discussed in Ref. [37].

[1] K. S. Novoselov, A. K. Geim, S. V. Morozov, D. Jiang, Y. Zhang, S. V. Dubonos, I. V. Grigorieva, and A. A. Firsov, Science **306**, 666 (2004).

[2] A. H. Castro Neto, F. Guinea, N. M. R. Peres, K. S. Novoselov, and A. K. Geim, Rev. Mod. Phys. **81**, 109 (2009).

[3] N. M. R. Peres, Rev. Mod. Phys. **82**, 2673 (2010).

[4] K. I. Bolotin, K. J. Sikes, Z. Jiang, M. Klima, G. Fudenberg, J. Hone, P. Kim, and H. L. Stormer, Solid State Commun. **146**, 351 (2008).

[5] M. Kumar, A. Laitinen, and P. Hakonen, Nat. Commun. **9**, 2776 (2018).

[6] K. S. Novoselov, A. K. Geim, S. V. Morozov, D. Jiang, M. I. Katsnelson, I. V. Grigorieva, S. V. Dubonos, and A. A. Firsov, Nature (London) **438**, 197 (2005).

[7] Y. Zhang, Y.-W. Tan, H. L. Stormer, and P. Kim, Nature (London) **438**, 201 (2005).

[8] S. Das Sarma, S. Adam, E. H. Hwang, and E. Rossi, Rev. Mod. Phys. **83**, 407 (2011).

[9] B. Zhou, K. Watanabe, T. Taniguchi, and E. A. Henriksen, Appl. Phys. Lett. **116**, 053102 (2020).

[10] R. P. Tiwari and D. Stroud, Phys. Rev. B **79**, 165408 (2009).

[11] J. Ping, I. Yudhistira, N. Ramakrishnan, S. Cho, S. Adam, and M. S. Fuhrer, Phys. Rev. Lett. **113**, 047206 (2014).

[12] S. Cho and M. S. Fuhrer, Phys. Rev. B **77**, 081402(R) (2008).

[13] A. L. Friedman, J. L. Tedesco, P. M. Campbell, J. C. Culbertson, E. Aifer, F. K. Perkins, R. L. Myers-Ward, J. K. Hite, C. R. Eddy, G. G. Jernigan *et al.*, Nano Lett. **10**, 3962 (2010).

[14] J. Bai, R. Cheng, F. Xiu, L. Liao, M. Wang, A. Shailos, K. L. Wang, Y. Huang, and X. Duan, Nat. Nanotechnol. **5**, 655 (2010).

[15] K. Gopinadhan, Y. J. Shin, I. Yudhistira, J. Niu, and H. Yang, Phys. Rev. B **88**, 195429 (2013).

[16] W. J. Wang, K. H. Gao, Z. Q. Li, T. Lin, J. Li, C. Yu, and Z. H. Feng, Appl. Phys. Lett. **105**, 182102 (2014).

[17] C. Chuang, Y. Yang, R. E. Elmquist, and C.-T. Liang, Mater. Lett. **174**, 118 (2016).

[18] A. Laitinen, M. Kumar, P. Hakonen, and E. Sonin, Sci. Rep. **8**, 594 (2018).

[19] C. Chuang, C. T. Liang, G.-H. Kim, R. E. Elmquist, Y. Yang, Y. P. Hsieh, D. K. Patel, K. Watanabe, T. Taniguchi, and N. Aoki, Carbon **136**, 211 (2018).

[20] G. Song, M. Ranjbar, and R. A. Kiehl, Commun. Phys. **2**, 65 (2019).

[21] J. Hu, J. Gou, M. Yang, G. J. Omar, J. Tan, S. Zeng, Y. Liu, K. Han, Z. Lim, Z. Huang *et al.*, Adv. Mater. **32**, 2002201 (2020).

[22] K. Gopinadhan, Y. J. Shin, R. Jalil, T. Venkatesan, A. K. Geim, A. H. C. Neto, and H. Yang, Nat. Commun. **6**, 8337 (2015).

[23] H. Li, Y. J. Zeng, X. J. Hu, H. H. Zhang, S. C. Ruan, M. J. Van Bael, and C. Van Haesendonck, Carbon **124**, 193 (2017).

[24] M. Kamada, A. Laitinen, W. Zeng, M. Will, J. Sarkar, K. Tappura, H. Seppä, and P. Hakonen, Nano Lett. **21**, 7637 (2021).

[25] D. V. Nomokonov, A. V. Goran, and A. A. Bykov, J. Appl. Phys. **125**, 164301 (2019).

[26] Y. Zheng and T. Ando, Phys. Rev. B **65**, 245420 (2002).

[27] M. Müller, L. Fritz, and S. Sachdev, Phys. Rev. B **78**, 115406 (2008).

[28] J. Jobst, D. Waldmann, I. V. Gornyi, A. D. Mirlin, and H. B. Weber, Phys. Rev. Lett. **108**, 106601 (2012).

[29] P. S. Alekseev, A. P. Dmitriev, I. V. Gornyi, and V. Y. Kachorovskii, Phys. Rev. B **87**, 165432 (2013).

[30] G. Y. Vasil'eva, P. S. Alekseev, Y. L. Ivanov, Y. B. Vasil'ev, D. Smirnov, H. Schmidt, R. J. Haug, F. Gouider, and G. Nachtwei, JETP Lett. **96**, 471 (2012).

[31] G. Vasileva, P. Alekseev, Y. Vasilyev, A. Dmitriev, V. Kachorovskii, D. Smirnov, H. Schmidt, and R. Haug, Phys. Status Solidi B **256**, 1800525 (2019).

[32] N. Tombros, A. Veligura, J. Junesch, J. Jasper van den Berg, P. J. Zomer, M. Wojtaszek, I. J. Vera Marun, H. T. Jonkman, and B. J. van Wees, J. Appl. Phys. **109**, 093702 (2011).

[33] See Supplemental Material at http://link.aps.org/supplemental/10.1103/PhysRevB.104.115432 for details of the theoretical model, additional theoretical considerations, and the effect of current annealing, which includes Ref. [47].

[34] A. Laitinen, M. Kumar, T. Elo, Y. Liu, T. S. Abhilash, and P. J. Hakonen, J. Low Temp. Phys. **191**, 272 (2018).

[35] A. Laitinen, G. S. Paraoanu, M. Oksanen, M. F. Craciun, S. Russo, E. Sonin, and P. Hakonen, Phys. Rev. B **93**, 115413 (2016).

[36] I. V. Gornyi, V. Y. Kachorovskii, and A. D. Mirlin, Phys. Rev. B **86**, 165413 (2012).

[37] E. H. Hwang, S. Adam, and S. Das Sarma, Phys. Rev. Lett. **98**, 186806 (2007).

[38] J. C. Meyer, A. K. Geim, M. I. Katsnelson, K. S. Novoselov, T. J. Booth, and S. Roth, Nature (London) **446**, 60 (2007).

[39] C. N. Lau, W. Bao, and J. Velasco, Mater. Today **15**, 238 (2012).

[40] I. V. Gornyi, V. Y. Kachorovskii, and A. D. Mirlin, Phys. Rev. B **92**, 155428 (2015).

[41] N. Shon and T. Ando, J. Phys. Soc. Jpn. **67**, 2421 (1998).

[42] P. M. Ostrovsky, I. V. Gornyi, and A. D. Mirlin, Phys. Rev. B **74**, 235443 (2006).

[43] G. Y. Vasileva, P. S. Alekseev, Y. B. Vasil'ev, A. P. Dmitriev, V. Y. Kachorovskii, D. Smirnov, H. Schmidt, and R. Haug, J. Exp. Theor. Phys. **129**, 438 (2019).

[44] A. Rycerz, Phys. Rev. B **81**, 121404(R) (2010).

[45] A. Laitinen, M. Kumar, and P. J. Hakonen, Phys. Rev. B **97**, 075113 (2018).

[46] B. T. Schaefer, L. Wang, A. Jarjour, K. Watanabe, T. Taniguchi, P. L. McEuen, and K. C. Nowack, Nat. Commun. **11**, 4163 (2020).

[47] A. A. Kozikov, A. K. Savchenko, B. N. Narozhny, and A. V. Shytov, Phys. Rev. B **82**, 075424 (2010).